Naval Research Laboratory

Washington, DC 20375-5320

NRL/MR/6410--06-8948

Computations of Chaotic Flows in Micromixers

Carolyn R. Kaplan
Junhui Liu
David R. Mott
Elaine S. Oran

Center for Reactive Flow and Dynamical Systems
Laboratory for Computational Physics and Fluid Dynamics

April 7, 2006

REPORT DOCUMENTATION PAGE

Form Approved
OMB No. 0704-0188

1. REPORT DATE *(DD-MM-YYYY)*	**2. REPORT TYPE**	**3. DATES COVERED** *(From - To)*
07-04-2006	Memorandum Report	

4. TITLE AND SUBTITLE

Computations of Chaotic Flows in Micromixers

5a. CONTRACT NUMBER

5b. GRANT NUMBER
64-6413-A-6

5c. PROGRAM ELEMENT NUMBER

6. AUTHOR(S)

Carolyn R. Kaplan, Junhui Liu, David R. Mott, and Elaine S. Oran

5d. PROJECT NUMBER

5e. TASK NUMBER

5f. WORK UNIT NUMBER

7. PERFORMING ORGANIZATION NAME(S) AND ADDRESS(ES)

Naval Research Laboratory
4555 Overlook Avenue, SW
Washington, DC 20375-5320

8. PERFORMING ORGANIZATION REPORT NUMBER

NRL/MR/6410--06-8948

9. SPONSORING / MONITORING AGENCY NAME(S) AND ADDRESS(ES)

10. SPONSOR / MONITOR'S ACRONYM(S)

11. SPONSOR / MONITOR'S REPORT NUMBER(S)

12. DISTRIBUTION / AVAILABILITY STATEMENT

Approved for public release; distribution is unlimited.

13. SUPPLEMENTARY NOTES

14. ABSTRACT

Three-dimensional simulations of the incompressible Navier-Stokes equations are used to examine the effects of repeating sequences of herringbone ridges in a microchannel. The calculations show how the presence of the structures leads to an asymmetrical pattern of transverse vortices in the velocity field, how this pattern repeats as the fluid moves over each similar sequence of ridges, how this velocity field stretches and folds fluid elements, and how this can lead to chaotic advection. A series of calculations with increasing numerical resolution show the varying rates of convergence of the flow velocity and passive-scalar convection and mixing as the fluid traverses more sequences. Mixing and convection are studied through traces of marker particles and through fluid convection of passive scalars, and these are compared. Numerical tests show the adequacy of structured grids and a new numerical algorithm for multidimensional incompressible flow. A methodology is developed and described that is used to assess accuracy and reduce the cost of such computations.

15. SUBJECT TERMS
Microfluidics
Staggered herringbone mixer
Chaotic advection

16. SECURITY CLASSIFICATION OF:			**17. LIMITATION OF ABSTRACT**	**18. NUMBER OF PAGES**	**19a. NAME OF RESPONSIBLE PERSON**
a. REPORT	**b. ABSTRACT**	**c. THIS PAGE**			Carolyn R. Kaplan
Unclassified	Unclassified	Unclassified	UL	39	**19b. TELEPHONE NUMBER** *(include area code)* (202) 767-2078

CONTENTS

COMPUTATIONS OF CHAOTIC FLOWS IN MICROMIXERS

1. Introduction

Components of microdevices containing fluids are now integral parts of micro-electro-mechanical systems. These microfluidic components are used to transport particles and reactants, and they are also used as chambers in which to perform various types of chemical and biological analysis. A general and critical problem in the design of microfluidic components is how to create a physical environment in which the movement and location of fluids (gases and liquids) and entrained particulates can be controlled for mixing, separation, and delivery. Sometimes it is just necessary to move two separate streams to some location, other times it is necessary to have two streams mixed to a certain degree at a specified site, and sometimes it is necessary to deliver a large particle in the flow to a specified surface for detection or modification. General and useful references include Ho (1998), Gad-el-Hak (1998, 2002), Karniadakis *et al.* (2002), Nguyen & Wereley (2002), and Breuer (2005).

In current terminology, a component is active when, for example, there are additional forces or driving mechanisms, such as mechanically driven parts, unsteady electric fields, or imposed oscillations in the inflow (see, for example, Evans *et al.* (1997), Rife *et al.* (2000), Glasgow & Aubry (2003), Tsai & Lin (2002), Ukita & Kanehira (2002), and Yang *et al.* (1998)). Often, but not always, this implied an attempt at active control of some property of the flow system. A passive component usually is one whose geometry is set before it functions, its parts do not move, and there are no additional fields or forces or time-dependent effects imposed on the system (see, for example, Bessoth *et al.* (1999), Park *et al.* (2004), Hong *et al.* (2004), Johnson *et al.* (2002), and Stroock et al. (2002)). In general, the first attempt is to design a passive system because it is simpler to design and requires less energy to operate.

When there is substantial internal structure in the channel or the component is passive, the flow can become chaotic (see, e.g., Jones *et al.* (1989); Khakhar *et al.* (1987); Ottino (1989); Wiggins & Ottino (2004); Chien *et al.* (1986); Kaplan *et al.* (2004, 2005)). Here the adjective chaotic is not meant in the colloquial sense of a state of extreme confusion and disorder. Rather, it is meant as it is used in nonlinear dynamics theory to mean a dynamical system that is extremely sensitive to its initial conditions, a system that produces complicated patterns that are not really random (e.g., Ottino (1990); Ottino & Wiggins (2004)). (We will go more into this later in the paper.) In this case, the velocity field itself can still be relatively straightforward to compute, but mixing and scalar transport become complex as a series of finer and finer striations form in time

Manuscript approved December 8, 2005.

or distance. Sometimes it is possible to use simplified models of nonlinear dynamics to analyze these flows, and these give important insights into the distinct regimes of the flow (e.g., Stroock & McGraw (2004); Khakhar *et al.* (1986)). A problem with totally relying on these models is that they are not usually quantitatively correct and might not be qualitatively correct in the presence of other physical effects such as molecular diffusion, thermal conduction, chemical reactions, or large particles in the flow. In this case, we can only use numerical simulation of the governing equations.

Liquids in microcomponents are characterized by low flow velocities, constant density, and hence low Reynolds numbers ($Re \approx 1 - 10$). The governing equations are the multispecies incompressible Navier-Stokes equations, generally including terms representing molecular diffusion, chemical reactions, and interphase drag and energy transfer. Thus the flow is laminar and often in the creeping flow regime. These equations are relatively straightforward to solve numerically when the chamber geometry is simple enough, the walls are relatively smooth or have well described functional behavior, and the component is passive. (That is, there are no external forces besides those which cause the material to flow at a constant rate through the chamber.) When these simplifications are not valid, obtaining the solution becomes extremely costly and time consuming.

This paper describes numerical simulations of a three-dimensional, geometrically complex, incompressible, "creeping" flow that is a prototype for one used in a micromixer. The original motivation for this work was to develop an affordable computational approach that would solve the Navier-Stokes equations accurately enough on a single workstation to design microfluidic components. Then, combined with new methods for rapid prototyping and testing, we could use the numerical model to determine, a priori, the best configurations. A major hurdle for computing many of these very low-Reynolds-number flows in complex geometries is resolving the effects of nonlinear dynamical processes, and determining how these complicate the flow structure. The difficulty of the problem is equivalent to that of turbulence in higher-Reynolds-number flows. As with turbulence, there are a number of low-order approaches, here based on nonlinear dynamics, for describing the effects of chaotic advection on mixing. The next-level problem, the one we are facing, is to understand the flow mechanistically and to develop methods to actually compute it and predict the behavior quantitatively as well as qualitatively.

This paper, a greatly extended expanded version of Kaplan *et al.* (2004), then describes our efforts to compute an incompressible flow that becomes more and more complex and convoluted, developing ever-narrowing striations of interpenetrating fluid as it moves downstream. Producing

our best result involved:

- Developing new numerical algorithms and approaches to computing incompressible flow that allow us to take advantage of the accuracy of nonlinear monotone methods for convection (Liu *et al.* 2005),
- Developing an approach to complex geometry that would not require paying the cost of unstructured grids, and
- Analyzing the flow, as the calculations evolved, so that we could take advantage of established physical properties of the flow, use a number of computational and theoretically motivated shortcuts, and still arrive at a reasonable final solution given current resources.

Here we use the Stroock *et al.* (2002) staggered-herringbone micromixer as a guide for testing the approach. They described their component as a microchannel containing a series of bas-relief herringbone structures (ridges in the channel) where one sequence consists of a total of twelve herringbone structures, six aligned one way, followed by six aligned oppositely. The channel in the original experiment consisted of 15 sequences, two of which are shown schematically in Fig. 1. This figure also indicates the dimensions used in the computations described later in this paper. Half of the liquid entering the channel contained a glycerol-water mixture (indicated by A) and half contained this same mixture with a small amount of light-sensitive fluoroscein dye (indicated by B). Images taken by Stroock *et al.* (2002) with a confocal micrograph, Fig. 2, show how striations of A and B form as the flow moves down the channel. By the time the fluid has passed the last sequence, it is effectively intermixed. Note that if the diffusion coefficient between A and B had been higher, better mixing would have occurred sooner.

2. Description of the Method

The physical model of the micromixer requires solution of the incompressible, multispecies Navier-Stokes equations,

$$\nabla \cdot \mathbf{v} \;=\; 0 \tag{1}$$

$$\frac{\partial \rho \mathbf{v}}{\partial t} + \nabla \cdot (\rho \mathbf{v}\mathbf{v}) \;=\; -\nabla P + \mu \nabla^2 \mathbf{v} \tag{2}$$

$$\frac{\partial c_i}{\partial t} + (\mathbf{v} \cdot \nabla c_i) \;=\; D_{i,j}\, \nabla^2 c_i, \qquad i = 1, n_s \tag{3}$$

where $\mathbf{v}$ is the fluid velocity, ρ is the fluid density, P is the pressure, μ is the dynamic viscosity coefficient, c_i is the concentration of component i of which there are n_s, and $D_{i,j}$ is the binary diffusion coefficient between two components i and j. These equations are solved on a three-dimensional Cartesian mesh using a finite-volume formulation with a colocated arrangement of variables (Liu *et al.* 2005). The advective fluxes are calculated with flux-corrected transport (FCT) (See Oran & Boris (2001) for details), using the package LCPFCT (Boris *et al.* 1993), which is a a high-order, nonlinear, monotone algorithm for solving continuity equations with source terms.

2.1 Tests of the Computations: Unperturbed Microchannel Flow

First consider a three-dimensional rectangular channel with the dimensions $4000 \times 90 \times 200$ μm^3, no obstacles in the flow, and smooth walls. (This is similar to that shown in Fig. 1, but without the ridges.) The channel contains water, characterized by a dynamic viscosity coefficient of 0.014 g/cm-s. The inflow velocity is specified at 1 cm/s, the outflow boundary condition is specified at 1 atm, and the walls are no-slip. Two passive scalars, labeled A and B, are introduced at the inflow. Scalar A represents water, B represents water with fluoroscein, and the binary diffusivity between A and B is taken as 1×10^{-6} cm^2/s. Scalars A and B follow the streamlines of the flow but do not interact with the fluid or each other. Here $Re \approx 1$.

Figure 3 shows the computed velocity profile in the x- and z-directions, pressure distribution, and concentration of B. The computational cells are 5 μm in all directions, so that there are $800 \times 18 \times 40$ computational cells in the grid. For this flow, boundary layers form along the microchannel walls where they grow, and merge, and eventually produce a parabolic pipe flow velocity profile. Along the centerline, the axial velocity accelerates to approximately 2 cm/s. After the start-up region, the steady state pressure gradient along the channel is linear and is 2950 dynes/cm3. The only signficant velocity in the z-direction is at the inflow boundary, due to the interaction of the fluid with the microchannel walls. At the inflow, the two fluids are completely unmixed. As the fluids move down the microchannel, there is a small amount of mixing at the interface due to mass diffusion. (This is seen by the slight spreading of the green area between the red and purple regions.)

Figure 4 shows these concentrations at the inflow and exit planes, $x = 0$ and 4000 μm, respectively. At the exit plane, the components are better mixed at the fluid interface at the upper and lower walls, $y = 0$ and $y = 90$ μm. This is because the fluid velocity is slowed considerably

along the walls, so that the two fluids have a longer residence time there during which they can diffuse and mix.

The results shown in Figs. 3 and 4 were obtained using 5 μm $\times$ 5 μm $\times$ 5 μm computational cells. Additional calculations at grid resolutions of 2.5 μm $\times$ 2.5 μm $\times$ 2.5 μm and 10 μm $\times$ 10 μm $\times$ 10 μm gave steady-state pressure gradients of 2925 and 3025 dynes/cm^3, respectively. From this essentially quadratic convergence, the steady-state pressure gradient is estimated as approximately 2912 dynes/cm^3. An analytic solution for the incompressible Navier-Stokes equations for flow in a rectangular-shaped duct is given by White (1991). Using the conditions appropriate for our simulation, the analytic solution predicts a steady-state pressure gradient of 2895 dynes/cm^3. Figure 5 shows a comparison of the x-velocity for point values of the analytic solution and cellaveraged values in the simulation for a grid resolution of 5 μm. The profile shows x-velocity along the y and z axes, in the region of fully developed flow.

2.2 Tests of the Computations: Effects of Staircased Grid

Because we are using a Cartesian grid and the herringbones are set at angles to the grid, we need to quantify the effects of staircasing on the solution. As an example of the tests we have performed, consider the problem shown in Fig. 6, flow over a triangular-shaped obstacle. The computational domain consists of $100 \times 20 \times 40$ cells, where each cell is 5 μm, corresponding to a domain of 500 μm $\times$ 100 μm $\times$ 200 μm. The obstacle is located in the region $200 < x < 250$ μm and $y < 35$ μm, and the staircasing is in the z-direction. In one test case, the obstacle staircasing is at the grid resolution (5 μm), and in another case, the staircasing is coarser, at 10 μm resolution.

Figure 7 shows results for the two cases at the $y = 25$ μm plane. Because this is such a highly viscous flow, there is essentially no difference in the two test cases. Figure 8 shows line profiles from this plane at $z = 100$ μm (along the centerline). The flat region in each profile, where $215 < x < 250$ μm, corresponds to the obstacle location. For these two cases, there are no differences in x-velocity, y-velocity and pressure, and only minor differences in z-velocity. From these and other similar tests (not shown), we conclude that with enough resolution, we should be able to use staircasing for these computations.

3. Computation of the Herringbone Mixer Flow

Channel flow is characterized by a pressure drop from the entrance to the exit. This is a function of channel length, cross-section, viscosity and flow rate. The total pressure drop along the length of the channel increases when there are obstacles present. The pressure drop is linear along the length of a channel for an incompressible fluid. Therefore, if we do not have any obstacles and we are given the pressure drop ($\partial p/\partial x$) across some segment of the channel, we then know the pressure drop across any segment. Below we show and use the fact that given a repeating sequence of obstacles, as we have with the herringbone patterns in Fig. 1, we can make an analogous statement about selected segments of the channel. Then we use this information to help decrease the cost of a many-segment calculation.

For idealized scalar transport, where there is no feedback from the scalars and the background flow, we can separate the problem into two types of computations. First, we compute the steady velocity field by solving the Navier-Stokes equations, and then we use this to compute the motion of the scalar field subjected to this velocity. By first obtaining the velocity field, we can vary how (that is, location, time history) passive scalars are injected. Knowing the velocity field is the key to understanding the flow in a geometry.

3.1 The Velocity Field

The inflow conditions and the dimensions of the herringbone mixer, as shown in Fig. 1, are the same as those of the microchannel with no obstacles. The individual herringbones are 20 μm in height, spaced 150 μm apart, and their surfaces in the flow are no-slip walls. The channel contains two sequences of herringbone structures, where each sequence consists of six herringbones with the short segment on the left and the long segment on the right, followed by six more herringbones with the short segment on the right and the long segment on the left. The ratio of the length of the long segment to short segment is 2:1. Results of grid resolution tests will be discussed throughout this paper, however, the velocity-field computations discussed in detail below are from an intermediate-resolution computation in which $\Delta x = \Delta y = \Delta z = 5$ μm, requiring $800 \times 18 \times 40$ computational cells for two sequences.

The major effect of the herringbone structures is to deflect the flow in a way that increases the interface area between the fluids and, therefore, allows enhanced mixing. As the inflowing fluid reaches the first herringbone, fluid at the bottom of the channel is deflected toward the vertical side

walls. A small portion is deflected one way (corresponding to the shorter segment) and a larger portion is deflected the other way (corresponding to the longer segment). As the fluid travels down each segment of the herringbone, it finally reaches the side walls and then is deflected up these walls, over the top of the microchannel (towards the center), and then down towards the bottom. The result is a flow pattern of two convective rolls forced by the geometry. This is best illustrated by velocity vectors, as shown in Fig. 9 at two cross sections. The larger convective roll is located on the side with the longer segment, while the smaller convective roll is on the side with the shorter segment. At $x = 600$ μm, the larger convective roll is on the left side of the channel, and at $x = 1540$ μm, the larger roll is on the right.

Figure 10 shows the velocity components at the longitudinal centerline, at $y = 45$ μm, which is approximately 20 μm above the herringbone structures. The x-velocity is similar to that in a pipe flow, with a boundary layer formed at the entrance. These boundary layers grow, merge, and form a fully developed pipe-flow profile. Effects of the herringbone structures can be seen in the x-velocity as it increases slightly above herringbones and decreases between these structures. The y-velocity increases when the fluid reaches a structure, and then decreases after it passes the structure. In other words, the ridges deflect the flow both out and toward the side walls and up, and then the the fluid flows down behind each ridge to fill the space between ridges. Similarly, the z-velocity component changes direction depending on the position of the fluid element in relation to the herringbone structure. This indicates that this is a highly viscous flow, driven by the herringbone structures; that is, the cross sectional flow stops when the structure ends. As shown in Fig. 10, the magnitude of the x-velocity is approximately a factor of ten greater than that of the y- and z-velocity components.

We see below that the velocity field becomes periodic in space as the flow progresses down the repeating herringbone sequences. The first sequence is the one that undergoes the most change, due to the proximity of the inflow boundary. This cycle effectively sets up the flow patterns. Subsequent cycles are essentially periodic, as shown in the cross section at the end of the first and second sequences in Fig. 11. If we assume that the velocity quickly becomes periodic, and we know that velocity field in the second or third sequence, the velocity field at any location in a sequence of herringbones is straightforward to calculate. Resolution tests with $\Delta x = \Delta y = \Delta z = 5$, 6, 7.5 and 10 μm (not shown) show that the velocity field for the 5 μm computational cell size is converged.

Given the smooth, resolved, and periodic velocity field, we are now able to examine the

advection of passive scalars in this field in more sequences than were computed for the velocity field. This periodicity of the velocity field reduces computational efforts significantly. These computations were done in two ways: first, by releasing and tracking tracer particles that move in a Lagrangian manner in the precomputed velocity field; and second, by using the fluid convection algorithm FCT to convect a passive-scalar density on the precomputed velocity field. These results can then be compared and assessed.

3.2 Particle Advection on the Velocity Field

The first approach we use to examine the effects of the velocity field on scalar transport is to consider the behavior of a set of Langragian tracer particles released in the flow. Tracer particles of species B are released in the flow on the right side. The equations solved for each particle j are:

$$\frac{dx_i^j}{dt} = u_i, \;\; i = 1, 2, 3 \;\; \text{and} \;\; j = 1, N \;, \tag{8}$$

where x_i^j and u_i^j are components of position and velocity, respectively. The boundary conditions are such that when a particle strikes a wall, it will stick to that wall and is removed from the calculation. No particle interacts with any other particle.

In the calculation described here, we have released 9000 particles on the right side of the inflow plane ($N = 9000$). This calculations uses the converged 5.0 μm-resolution velocity field. At the inflow, twenty-five evenly spaced particles (5×5) were released in each computational cell. Figures 12-15 show selected particle traces through the four sequences. Each figure shows two views: a three-dimensional rendering that shows how the particle moves across the ridges, and a two-dimensional projection of the particle motion on the $y - z$ plane. These four figures describe very different types of particle paths. Figure 12 shows the path of a particle that starts out on the right side and stays on the right. It oscillates a little as it moves downstream, but it stays within a small region of the $y - z$ plane. Figure 13 is a very different case. The particle starts out on the right side and, by the end of the first cycle, is far over on the left side. Figure 14 shows the track of a particle that stays in essentially the same location on the $y - z$ plane until early in the second sequence, when it abruptly moves over to the left side. The final example, Figure 15, shows a particle that has become trapped at a wall.

Figure 16 shows planes at the end of each sequence, with white dots indicating where a B particle has intersected that plane. These figures result from a one-time particle release and not

a continuous stream. Therefore, the time that each particle intersects a particular plane could be quite different. A striking feature of the frames in Fig. 16 is that the shapes of the B regions on the left look as though they have been lifted and removed from the right side. In fact, as we show next, they have been stretched and folded and almost pulled out. An important point here is that we cannot really decipher the dynamics or the fluid evolution as it moves downstream from these pictures alone. What we can see is an overall outline of the shape of the regions of B.

There are several sources of numerical error in these particle traces. The first type is the residual error inherent in the computation of the velocity field, which is small, and to high precision $\nabla \cdot \mathbf{v} \simeq 0$. Other errors in the particle computations could arise in the specific velocity field used for some of the particles. All particles in a particular computational cell were convected with the velocity field computed for that cell center, regardless of where in the cell a particle was located. This is consistent with the velocity-field calculation. Another option would have been to use an interpolated velocity field for each location of each particle, which, in turn, could introduce interpolation errors.

3.3 Convection of a Continuous Variable

Now consider a different diagnostic approach. Above we used discrete particles and tracked their paths in the flow. Now we consider a continuous representation and convect a passive-scalar density on the same fixed, precomputed velocity field. Passive scalar densities were convected for the 5 μm resolution discussed above, as well as for a 2.5 μm and 1.25 μm resolution. The computations at 2.5 μm and 1.25 μm resolution were done using a velocity field that was interpolated from the converged velocity field on the 5 μm grid. Figure 17 shows snapshots of passive scalars for two full sequences of herringbone structures, computed at 1.25 μm resolution. The number on each image corresponds to the plane immediately after that structure. (That is, 1 corresponds to the plane immediately after the first herringbone, and there are 12 structures in a sequence.) These images were obtained by solving equation

$$\frac{\partial \phi_k}{\partial t} + \mathbf{v} \cdot \nabla \phi_k \;=\; 0, \quad k = A, B \tag{9}$$

where ϕ_k is the scalar density of species A or B, and $\mathbf{v}$ has been previously computed. Because the mass diffusion term had negligible effect in the computations, we did not use it in the computations shown now. There is a zero-gradient boundary condition for A and B at the walls and at the

outflow. (This is physically different from the boundary condition used on tracer particles at walls, where a tracer particle that hits a wall was stuck to that wall and did not move any further.) At the inlet, there is a continuous inflow of B on the right side. The multidimensionality was handled by direction splitting the convection algorithm (Oran & Boris 2001).

For an incompressible flow, the total flux in each (y, z)-plane,

$$\iint_{(y,z)\ \text{plane}} \phi_k \, u \, dy \, dz$$

is conserved in the x direction. Because the value of ϕ_k in each computational cell on the inflow plane is either 0 or 1, the values of ϕ_k in every other downstream cell in the domain are limited, $0 \leq \phi_k \leq 1$ because of the conservation of ϕ_k expressed by Eq. (9). Values of ϕ_k can be less than 1 in a computational cell because a fluid element could be distorted by the flow so that at a later time, its (constant but distorted) volume covers portions of several adjacent computational cells. When that happens, we say that the cell is mixed and the density of ϕ_k is less than 1. Checking conservation and the bounds of ϕ_k is a standard way to check the accuracy of this computation.

At the inflow (marked Start) shown in Fig. 17, red fluid, ϕ_B, enters on the right side, and purple fluid, ϕ_A, enters on the left side. For the first six herringbones, the larger convective roll forms on the left side. Therefore, purple fluid is pushed towards the right near the top of the microchannel, while red fluid is pulled towards the left near the bottom. When the herringbone pattern is reversed (structures 7 through 12), the red fluid is pushed upwards and over to the left at the top, while purple fluid is pulled towards the right near the bottom. At the end of the first sequence of herringbones (after structure 12), some of the red fluid has traveled to the left side, and some of the purple fluid has travelled to the right side. This flow pattern repeats itself during the second full cycle of structures, herringbones 13 – 24.

The convection of passive scalar densities at 5 μm, 2.5 μm and 1.25 μm resolutions were also carried out for four full sequences. The periodic feature of the velocity field was used to obtain the velocity field of the third and fourth sequence. Computing four full sequences at 2.5 μm resolution required $3200 \times 36 \times 80$ computational cells, and at the 1.25 μm resolution required $6400 \times 72 \times 160$ computational cells. These computations were done with a fully parallelized version of a fluid convection code, and required approximately 10 hours of wall clock time on 40 processors of an SGI Origin 3800 for the 2.5 μm resolution and 22 hours of wall clock time on 160 processors for the 1.25 μm resolution.

Figure 18 compares the computations at the end of four sequences for the 5 μm, 2.5 μm and 1.25 μm resolutions. For any fixed resolution (looking down any column in Fig. 18), we see that the structure of ϕ_B becomes more and more complex as we move downstream and pass more sequences of herringbones. The structure of ϕ_B eventually evolves into the types of striations seen in the experiment. This behavior has been called "chaotic advection," described as the complex behavior shown by a passive scalar (a fluid particle or element, or a passively advected quantity such as temperature or concentration of a second tracer fluid) when it is driven by Lagrangian dynamics in the flow (Cartwright *et al.* 1999).

Now consider the plane at the end of sequence 1 for the three resolutions. (This means looking at the top row of the three columns.) From these figures, we can see the shapes of regions that evolve as the accuracy increases. This can also be said of the planes of at the end of sequences 2, 3, and 4. Lower resolutions are not adequate as the striations become finer and finer, but they do show how the structures will evolve at downstream locations.

The right-most column of Fig. 18 shows the end of the first four sequences for the most resolved computation of ϕ_B, at 1.25 μm resolution. Scalar B particles moved across the channel, from the right to the left side, and this material appears as striations in the flow. What is particularly interesting about this flow is how misleading it can be to look at these planes alone, without knowing how the flow has evolved as it moves downstream. To make this point, we have reproduced these cross sections in Fig. 19, and labeled the regions of B on the left side as a, b, c, and d. For example, one interpretation might be that material in a, shown at the end of sequence 1, is the same material that is shown at b, at the end of sequence 2. We have shown that this is not true by looking at intermediate pictures (such as in Fig. 17) and an animation of the evolution of the flow as it moves downstream. These show that material a at the end of each sequence is essentially the same material marked a at the end of earlier sequences. And the same is true of b, c, and d. That is, as new islands of material form on the left hand side, the existing islands move up and towards the center.

There are several sources of error in the computations shown in Figs. 17 and 18. First, there is the residual error in the computation of the velocity field, but we know that this is negligibly small. Other errors arise in the actual solution of Eq. (9). There is some error introduced in the solution of ϕ_B by numerical diffusion, even though FCT is a high-order algorithm. In the cases of the computations on finer resolution grids, shown in Fig. 18, there is also some error introduced

by the interpolation of the velocity field onto finer grids.

3.4 Comparison of Particle Tracks and Continuous Convection

Figures 16 and 19 can now be compared, and we can use the intermediate results of Figs. 12-15 and Fig. 17 to provide additional information. In addition, we have an animation that gives us details of how the flow and scalars change as we step through the computational domain. (This is available on request.)

There are strong similarities in the structures in Figs. 16 and 19, which is both encouraging and useful. Both approaches show the striations forming as the tracer particles or scalar variable moves through various sequences. If either Fig. 16 or 19 were all that we needed, we could obtain it in a much less expensive way by doing particle traces, rather than by convecting the scalar B. Differences are apparent around the walls, and these differences are consistent with the differences in boundary conditions in the two types of calculations. That is, in the particles traces, those particles that approach a wall are essentially trapped there, whereas they can eventually escape in the scalar convection calculation.

A striking feature of the frames in Figs. 16 and 19 is that the shapes of the B regions on the left look as though they have been lifted and removed from the right side. The history of these islands of B, however, and not just their final shapes, are critically important in evaluating the performance of the mixer, particularly when the component is applied to real mixing problems with finite mass diffusion. The question is whether B in these islands has always been near the $A-B$ interface or if this B material is close to A only after each island is formed. If these islands consist of material that had previously been adjacent to the right wall, then this material B was isolated from material A until the mixer pulled it to the left and placed it in close proximity to A. This displacement of fluid B would produce huge concentration gradients in the diffusing species and rapid mass transfer between the fluids at the islands. If, in contrast, the material in the islands originates near the $A-B$ interface, then mass diffusion would have already smoothed the gradient between the two fluids, and the mass transfer at the island would be reduced.

To understand how these regions form, we examined the dynamics of this flow. This was done by looking at the evolution of B as the flow moved over the sequences of structures. We found that the material marked a in Fig. 19 was originally on the interface between A and B at the inflow. Then as the material passed over later sequences, regions b, c, and d were, in turn, moved from the

$A-B$ interface. These regions of material were stretched, folded, and ultimately pinched from the larger B region along the $A-B$ interface. This evolution can also be seen in Fig. 17. Starting at herringbone 1, red fluid from the $A-B$ interface is moved over to the left along the bottom of the channel for the first six herringbones. Then, when purple fluid is moved over to the right along the bottom of the channel for the second six herringbones, the red fluid on the left (from the $A-B$ interface) is pinched off from the larger B region, resulting in the island of red fluid on the left hand side at the end of the first sequence (Herringbone 12). This movement of material is confirmed by selected particle tracks, but the advection of the continuous scalar concentration demonstrates this evolution much more clearly.

4. Comments and Conclusions

Mixing, due to enhanced stretching, bending, and folding of material surfaces in a flow, has been studied extensively in systems that show chaotic advection. Mixing, however, is only one part of the problem. We are also interested generally in flow control, and that includes mixing, separation, delivery, and transport. The development of concepts of nonlinear dynamics can be helpful in all of these areas. In terms of nonlinear dynamics, a fixed point in the system is one in which a particle starts out at some point (x_o, y_o, z_o) and remains for all time t at (x, y_o, z_o). The particle travels in a straight line through the system. A periodic point is one in which a particle released will return to its initial position, again and again, after a fixed time or space interval. At intermediate times, it is elsewhere, and could be anywhere. What is important is that you know when to find it at the specified point, and in our case, we know where it has been. Sometimes, there are periodic points but their period is longer — it takes more cycles for the particle to return to its initial point.

Passive scalars, as those shown in Figs. 12–19, are particles that are not large enough to perturb the flow, but large enough not to diffuse (that is, there is no Brownian motion). As such, they only approximate the motions of real, and often relatively large particles of interest in a background flow. Our velocity field is steady, but periodic in space. Therefore, we could, in principle, look for fixed points and periodic points in the flow. Figure 16 is a Poincaré map, a reduction in the dimension of the system found by using a section of the flow (in time or space) to produce a map. The dynamic behavior of this map is sometimes easier to study than the full system, and sometimes gives some useful insights into the system. For example, the particle shown in Fig. 12 is close to a fixed point. Other points might be close to periodic points. In general,

however, we seem to learn more about the dynamics of the system and the physical mechanisms of the flow by focusing on the fluid elements and particle motions in three dimensions.

In the experiment (Fig. 2), a laser aimed at the liquid containing the light-sensitive dye provided visualization of the mixing between the two streams. Note that the visualization was not calibrated – we do not know exactly how much mixing corresponded to a certain intensity of light. The scale could have been linear, or simply a sharp cut off, or some highly nonlinear function. In addition, the laser experiments were affected by light reflection from the walls. This would make the signal appear stronger near the walls. This was indicated to some extent in the experimental paper, which used only an inner portion of the image (the part enclosed by the dashed lines in Fig. 2) for the analysis. Finally, at a relatively late stage in our work, we learned that the experimental herringbones are actually grooves in the channel, not ridges protruding into the channel flow (Stroock *et al.* (2002); Stroock & McGraw (2004)), as was simulated here. However, given this, and comparing Figs. 2 and 18, we can conclude that grooves and ridges produce similar qualitative effects at the scales in which we are looking.

Numerical resolution is an important issue here. We really cannot resolve the striations that form after multiple sequences in any reasonable amount of computer time. Then we ask: do we really need to do this? It is unlikely that practical devices will need more than a few sequences, and recent studies (Howell *et al.* 2005) have shown that by varying the pattern ridges or grooves, we can achieve mixing and flow control in much shorter distances than 15 cycles or even four cycles. In any case, we can compute $\mathbf{v}$ to high enough accuracy, and this is really the beginning of the problem. We can use this $\mathbf{v}$ to study the dynamics, as long as the particle-fluid interactions are small and do not affect $\mathbf{v}$. When these interactions do affect $\mathbf{v}$, the computations of $\mathbf{v}$ and the particle behavior must be done simultaneously and interactively, more as it is done in multispecies or multiphase fluid dynamcis.

A major conclusion, then, is that we were really not able to analyze and fully understand the flow from the particle traces alone. Without considering the details of the flow evolution, which were obtained from the passive scalar advection, we could not understand how certain parts of scalar B were moved across the channel. These clarified what we saw in the particle traces. Both approaches, however, provided valuable information and were used to back up or substantiate the conclusions.

Acknowledgments

This work was funded by the Office of Naval Research. The authors acknowledge extensive conversations with Dr. Abe Stroock to help us understand his experiments, Dr. Jay Boris who gave us many insights into the numerical approach and the methodology we developed, Drs. Frances Ligler and Peter Howell in NRL's Center for Biomolecular Science and Engineering who provided insights into microfluidic mixing and component design, and Dr. Rowena Ball who provided insights into nonlinear dynamics that were useful in interpreting the results.

References

Bessoth, F.G., deMello, A.J. & Manz, A. 1999 Microstructure for efficient continuous flow mixing *Anal Commun,* **36**, 213–215.

Boris, J.P., Landsberg, A.M., Oran, E.S. & Gardner, J.H. 1993 LCPFCT — A Flux-Corrected Trasport algorithm for Solving Generalized Continuity Equations, NRL Memorandum Report 6410-93-7192, Naval Research Laboratory, Washington, DC.

Breuer, K. 2005 Microscale Diagnostic Techniques, Springer, Heidelberg.

Cartwright, J.H.E., Feingold, M. & and Piro, O. 1999 An introduction to chaotic advection, 307–342, in Chaos and Turbulence, ed. Chaté et al., Kluwer Academic, NY.

Chien, W.L., Rising, H., & Ottino, J.M. 1986 Laminar mixing and chaotic mixing in several cavity flows *J. Fluid Mech.* **170**, 355–377.

Evans, J., Liepmann, D. & Pisano, A.P. 1997 Planar laminar mixer *Proc. IEEE 10th Annual Workshop of Micro Electro Mechanical Systems (MEMS '97)*, Nagoya, Japan 1997, 96–101.

Gad-el-Hak, M. 1998 The fluid mechanics of microdevices *J. Fluids Eng.* **121**, 5–33.

Gad-el-Hak, M. 2002 The MEMS Handbook, CRC Press, Boca Raton, FL.

Glasgow, I. & Aubry, N. 2003 Enhancement of microfluidic mixing using time pulsing *Lab on a Chip* **3**, 114–120.

Ho, C.-M. & Tai, Y.-C. 1998 Micro-electro-mechanical systems (MEMS) and fluid flows *Annu. Rev. Fluid Mech.* **30**, 539–578.

Hong, C.-C., Choi, J.-W. & Ahn, C.H. 2004 A novel in-plane passive microfluidic mixer with modified Tesla structures *Lab on a Chip* **4**, 109–113.

Howell, P.B., Mott, D.R., Fertig, S., Kaplan, C.R., Golden, J.P., Oran, E.S. & Ligler, F.S. 2005 A Microfluidic Mixer with Grooves Placed on the Top and Bottom of the Channel *Lab on a Chip* **5**, 524–530.

Johnson, T.J., Ross, D. & Locascio, L.E. 2002 Rapid microfluidic mixing *Anal. Chem.* **74**, 45–51.

Jones, S.W., Thomas, O.M. & Aref, H. 1989 Chaotic advection by laminar flow in a twisted pipe, *J. Fluid Mech.* **209**, 335–357.

Kaplan, C.R., Mott, D.R. & Oran, E.S. 2004 Towards the design of efficient micromixers, AIAA Paper 2004-0931, AIAA, Reston, VA.

Kaplan, C.R., Oran, E.S., Mott, D.R. & Liu, J. 2005 Computations of Chaotic Flows in Micromixers, *2005 NRL Review*, p. 219-221, Naval Research Laboratory, Washington, DC.

Karniakakis, G., Beskok, A. & Aluru, N. 2002 Micro Flows Fundamentals and Simulation, Springer, New York, NY.

Khakhar, D.V., Rising, H. & Ottino, J.M. 1986 Analysis of chaotic mixing in two model systems, *J. Fluid Mech.* **172**, 419–451.

Khakhar, D.V., Franjione, J.G. & Ottino, J.M. 1987 A case study of chaotic mixing in deterministic flows: the partitioned-pipe mixer *Chem. Engng. Sci.* **42**, 2909–2926.

Liu, J., Mott, D.R., Kaplan, C.R. & Oran, E.S. 2006 Application of FCT to Incompressible Flows, NRL Memorandum Report 6410–06-8947, Naval Research Laboratory, Washington, DC.

Nguyen, N.-T. & Wereley, S.T. 2002 Fundamentals and Applications of Microfluidics, Artech House, Norwood, MA.

Ottino, J.M., 1990 Mixing, chaotic advection, and turbulence, in *Annu. Rev. Fluid Mech.* **220**, 207–253.

Ottino, J.M. & Wiggins, S. 2004 Introduction: mixing in microfluidics, *Phil. Trans. R. Soc. Lond.* A **362**, 923–970.

Ottino, J.M. 1989 The Kinematics of Mixing: Stretching, Chaos, and Transport, Cambridge University Press, NY.

Oran, E.S. & Boris, J.P. 2001 Numerical Simulation of Reactive Flow, 2nd ed. Cambridge University Press, Cambridge.

Park, S.J., Kim, J.K., Park, J., Chung, S., Chung, C. & Chang, J.K. 2004 Rapid three-dimensional passive rotation micromixer using the breakup process *J. Micromech. Microeng.* **14**, 6–14.

Rife, J.C., Bell, M.I., Horwitz, J.S., Kabler, MN, Auyeung, R.C.Y. & Kim, W.J. 2000 Miniature valveless ultrasonic pumps and mixers. *Sensor Actuat. A - Phys.* **86**, 135–140.

Stroock, A.D. & McGraw, 2004 G.J., Investigation of the staggered herringbone mixer with a simple analytical model, *Phil. Trans. R. Soc. Lond.* A **362**, 971–986.

Stroock, A.D., Dertinger, S.K.W., Ajdari, A., Mezic, I., Stone, H.A. & Whitesides, G.M. 2002 Chaotic mixer for microchannels, *Science* **295**, 647–651.

Tsai, J.H. & Lin, L.W. 2002 Active microfluidic mixer and gas bubble filter driven by thermal bubble micropump. *Sensor Actuat. A-Phys.* **97-8**, 665–671.

Ukita, H. & Kanehira, M. 2002 A shuttlecock optical rotator – Its design, fabrication and evaluation for a microfluidic mixer 2002 *IEEE J. Sel. Area Comm.* **8**, 111–117.

White, F.M. 1991 Viscous Flows, p. 120, McGraw Hill, NY.

Wiggins, S. & Ottino, J.M. 2004 Foundations of chaotic mixing *Phil. Trans. R. Soc. Lond.* A **362**, 937–970.

Yang. Z., Goto, H., Matsumoto, M. & Yada, T. 1998 Micro mixer incorporated with piezoelectrically driven valvless micropump *microTAS 1998*, 177–180.

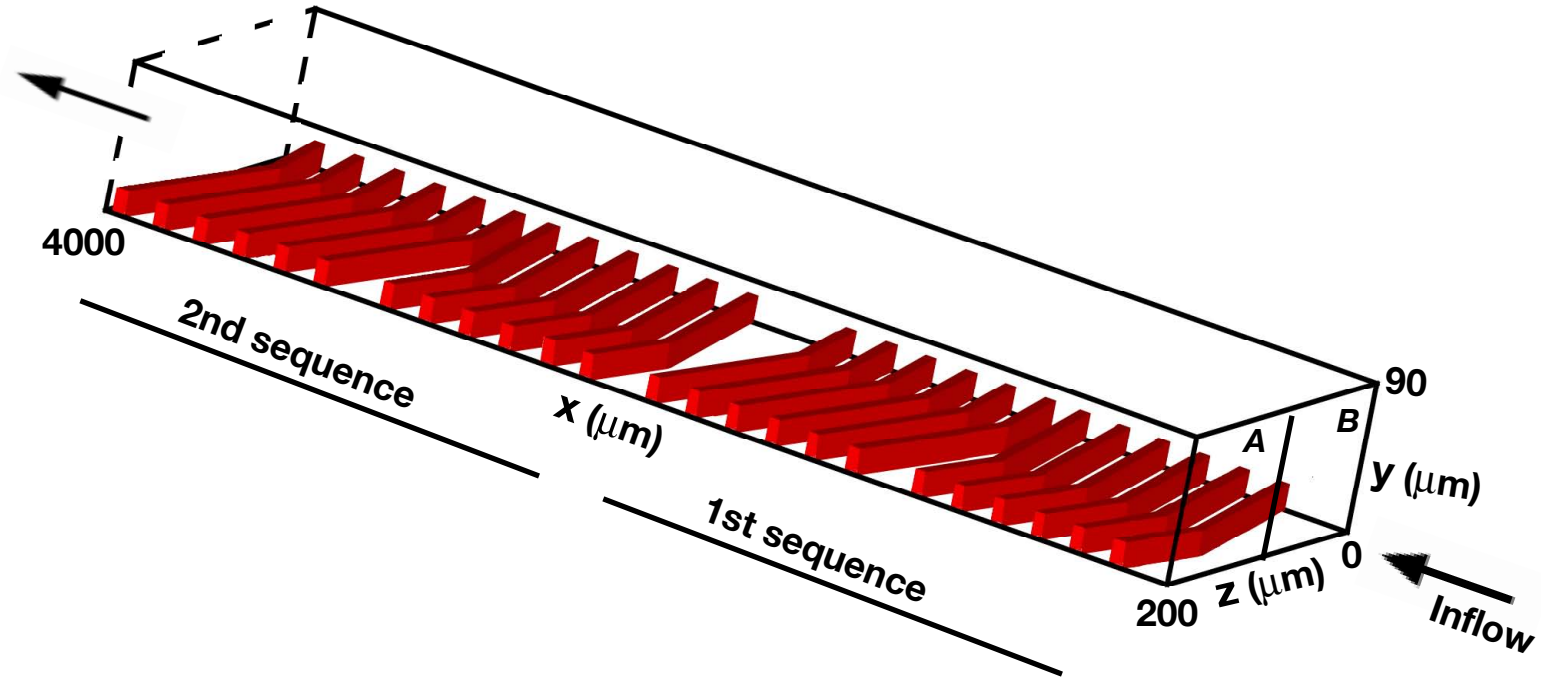

Figure 1. Schematic of a microchannel with herringbone ridges. The first two sequences are shown.

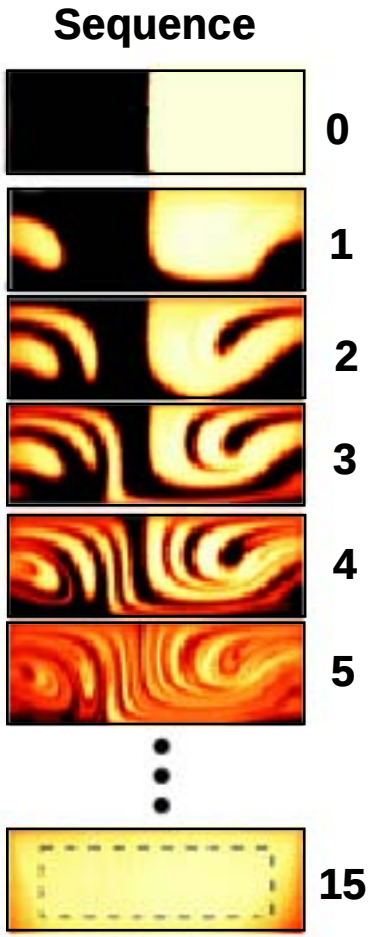

Figure 2. Confocal micrograph images taken at the end of the first five sequences and the last sequence (*Stroock et al. (2002)*).

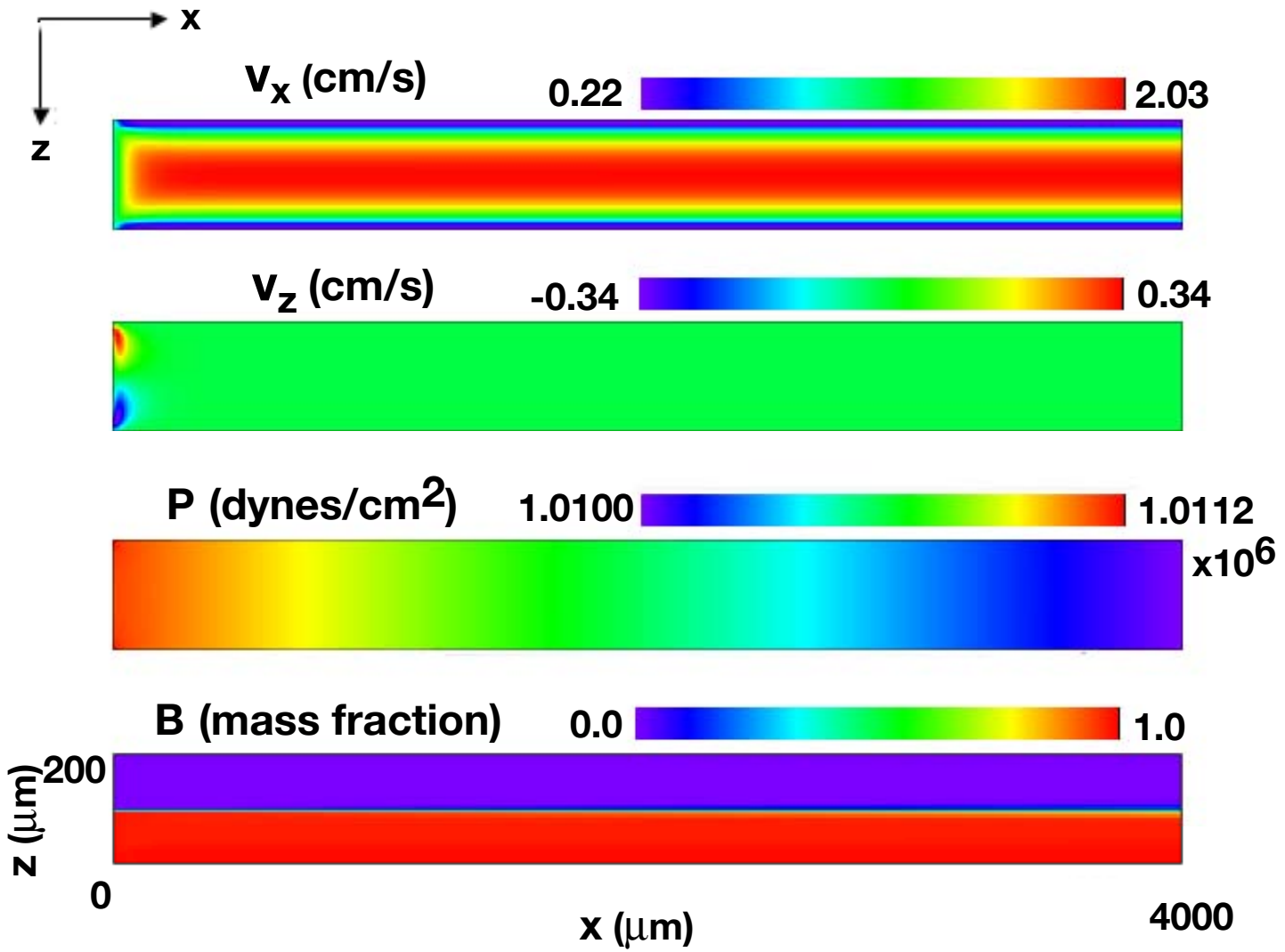

Figure 3. Computed x-velocity, z-velocity, pressure, and concentration of B in the x-z plane at $y = 45$ μm for the unobstructed microchannel.

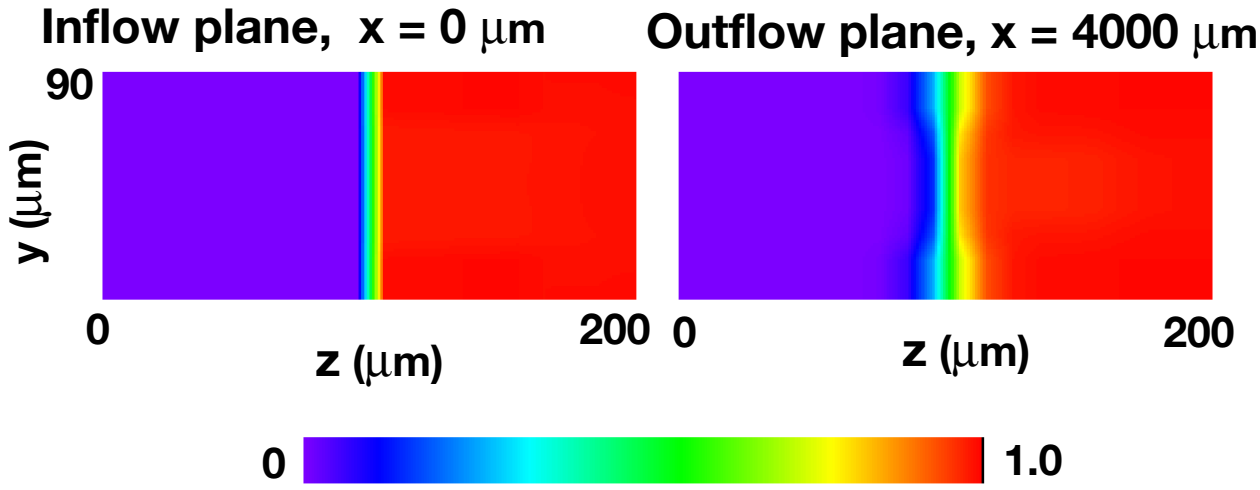

Figure 4. Concentrations of scalars A and B at the inflow (x = 0 μm) and exit (4000 μm) planes, respectively, for the unobstructed microchannel.

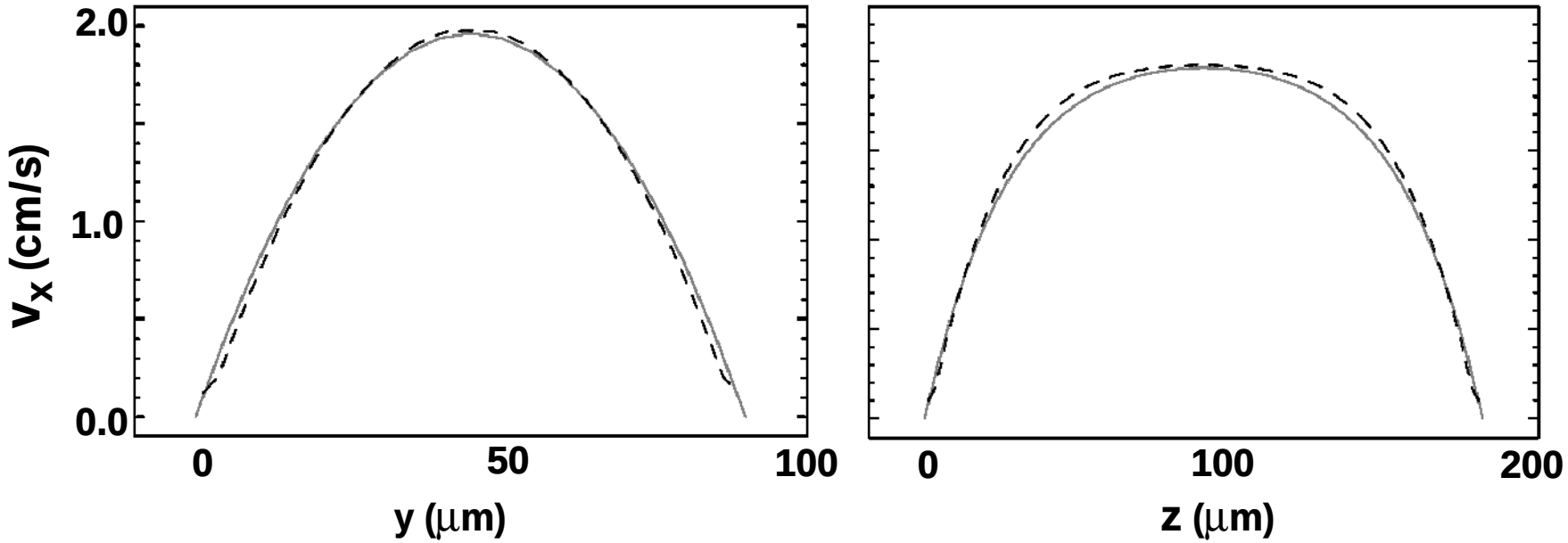

Figure 5. Comparison of the analytic solutions for the x-velocity (solid curve) to those from the simulation at a grid resolution of 5 μm (dashed lines) in a fully-developed region of the flow.

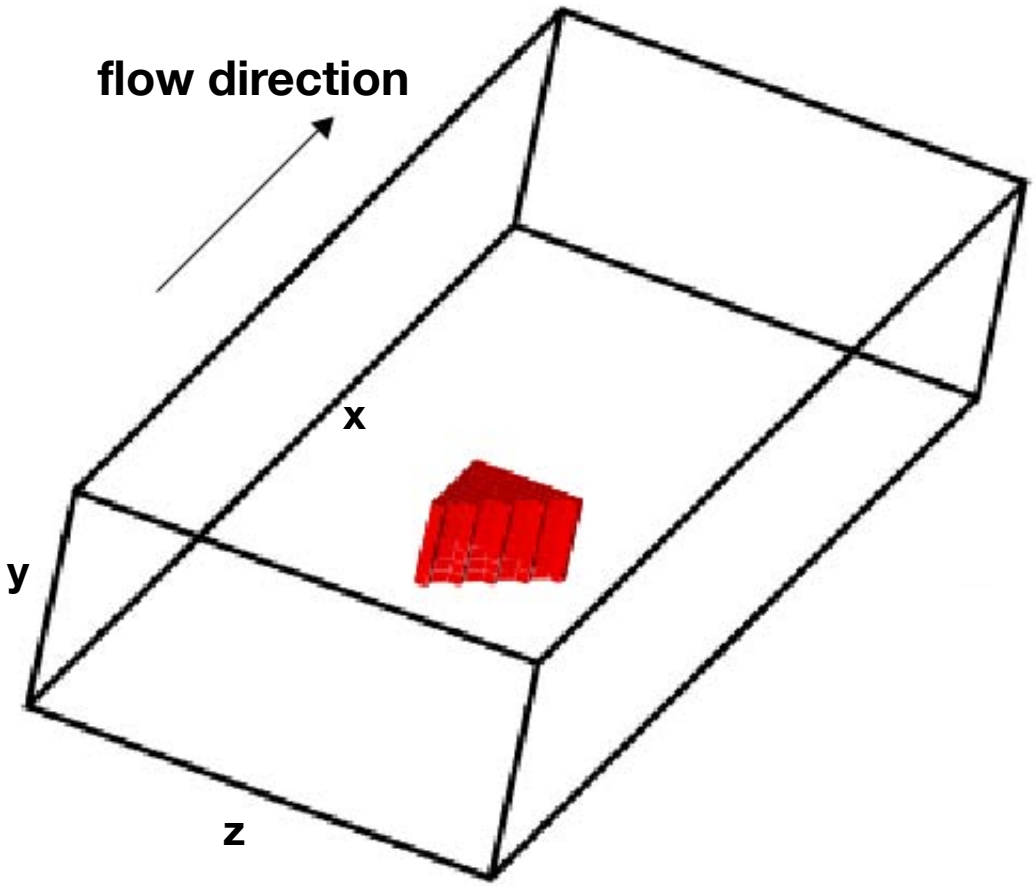

Figure 6. Example of the tests performed to evaluate the effects of staircasing in the computational grid. A triangle-based obstacle is placed in the flow, with staircasing in the z-direction.

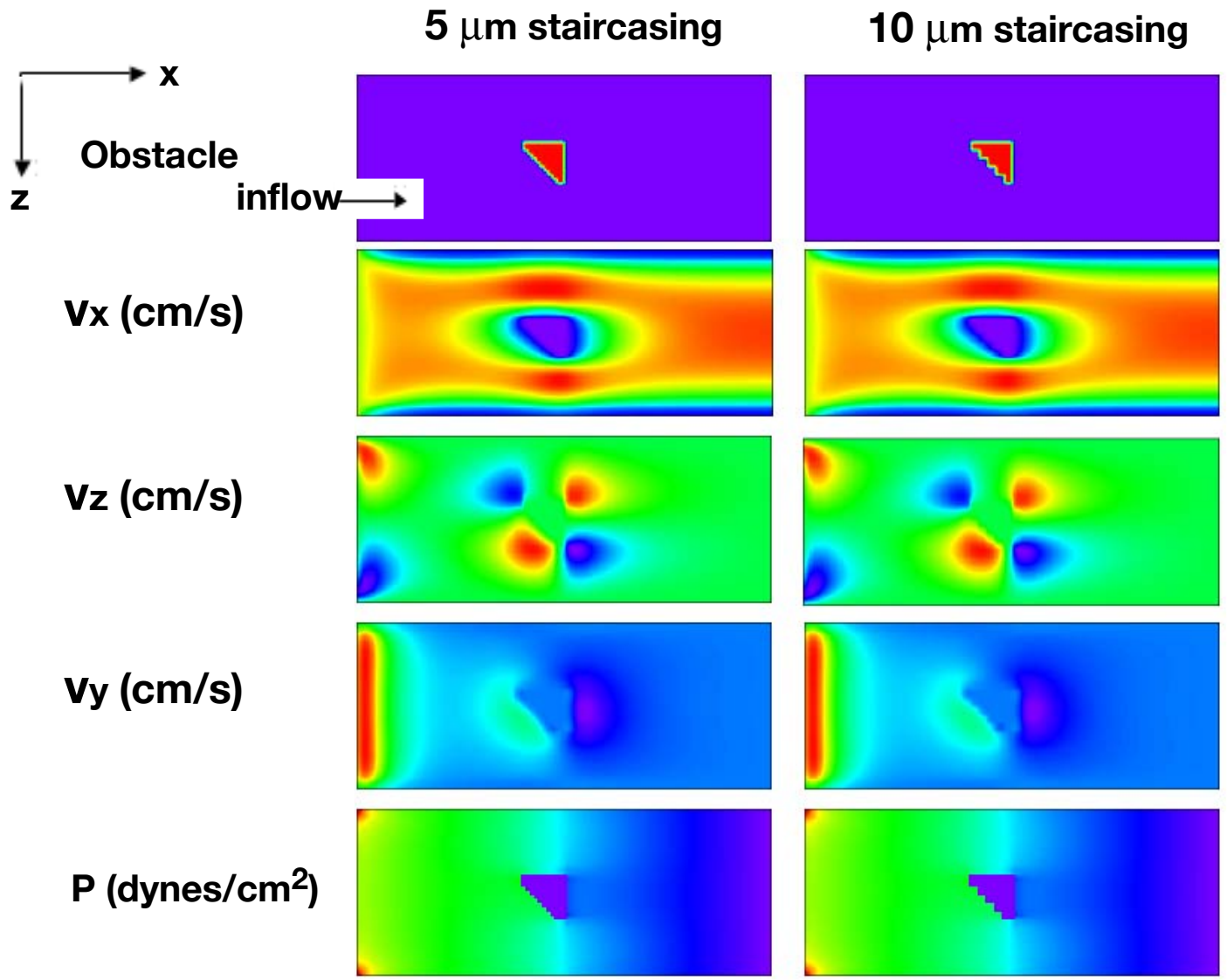

Figure 7. Geometry, computed velocities, and pressure for the obstacle shown in Figure 6. Quantities are shown in the x - z plane at y = 25 μm for the two staircasing resolutions.

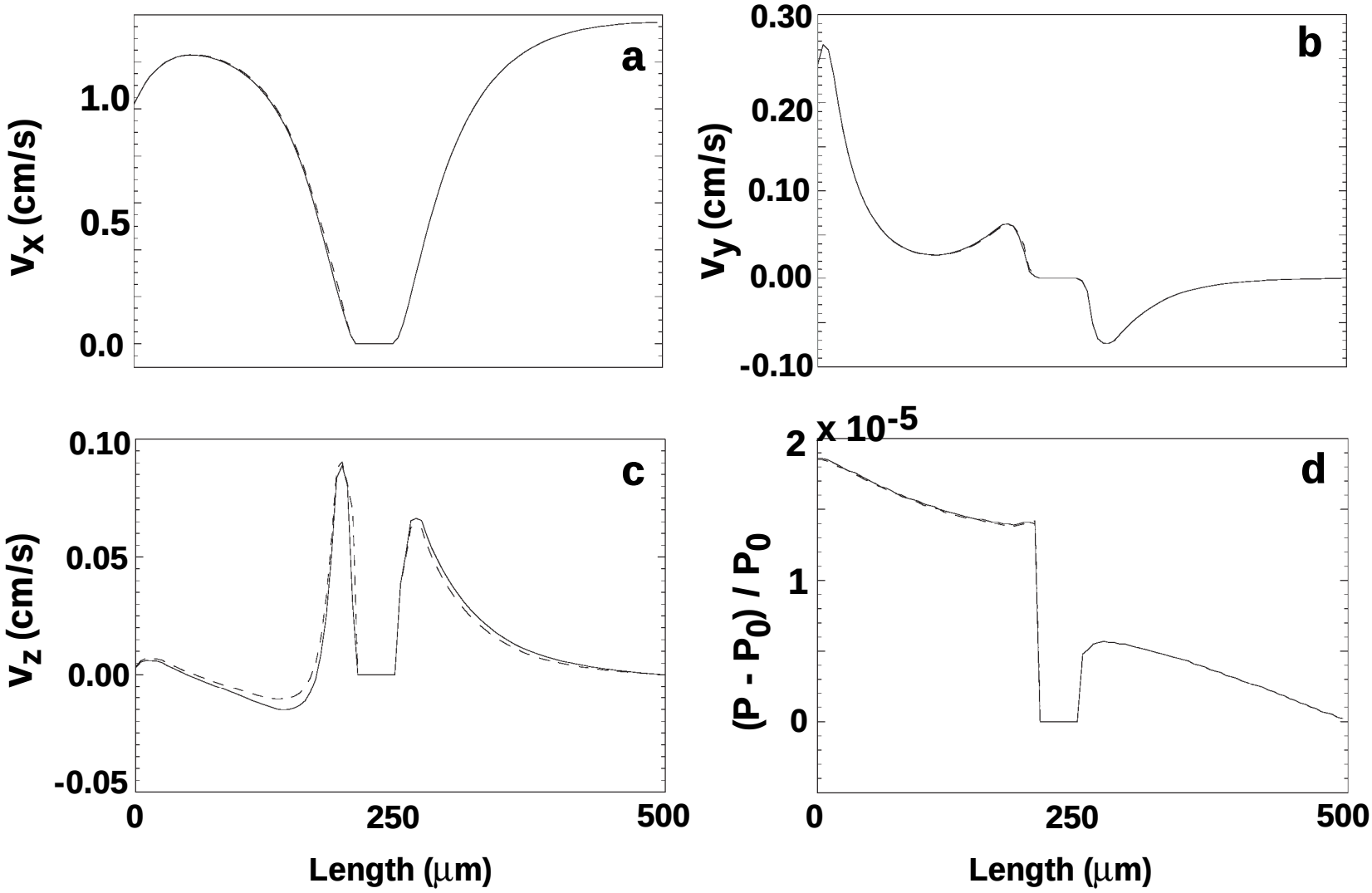

Figure 8. Profiles along the x-axis, at $y = 25$ μm, $z = 100$ μm for the two staircasing resolutions. The flat region in each profile, where $215 < x < 250$ μm, corresponds to the obstacle location.

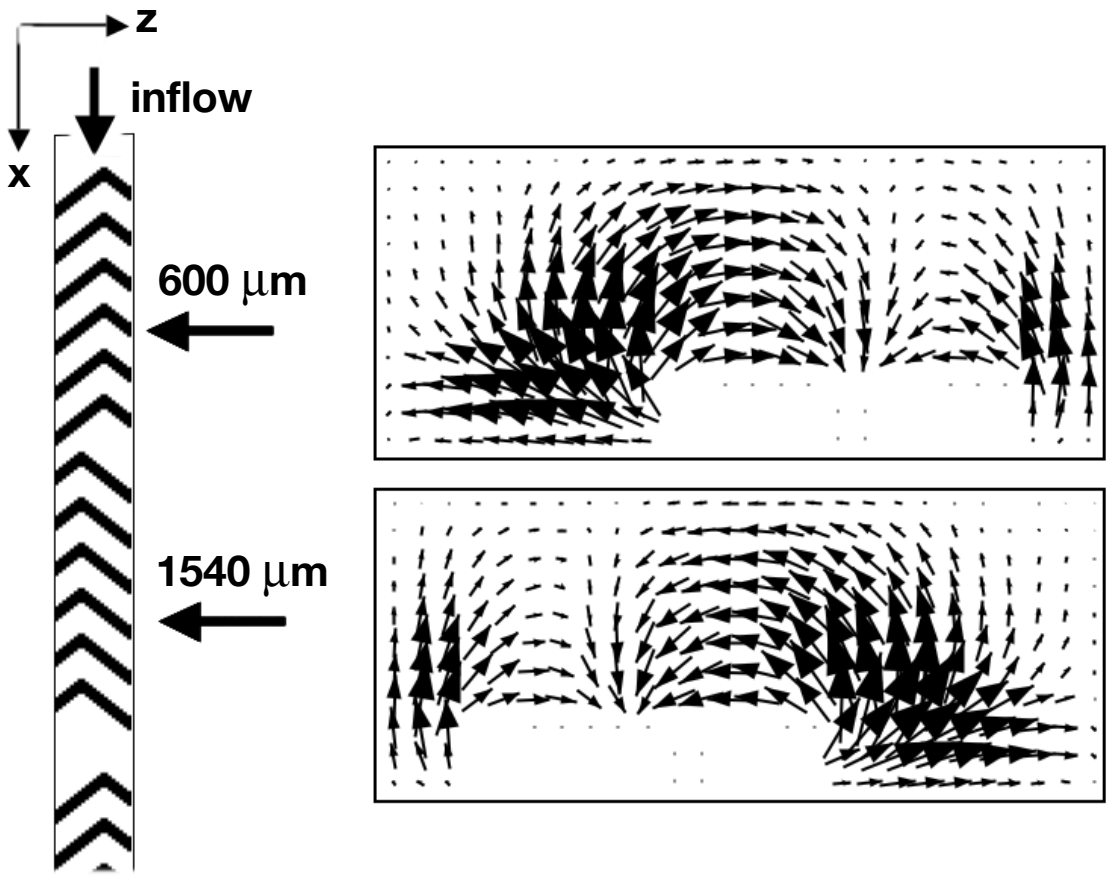

Figure 9. Velocity vectors in the y - z plane showing the flow pattern of geometry-induced convective rolls in the cross section of the microchannel shown in Fig. 1 at two x-locations, 600 μm and 1540 μm.

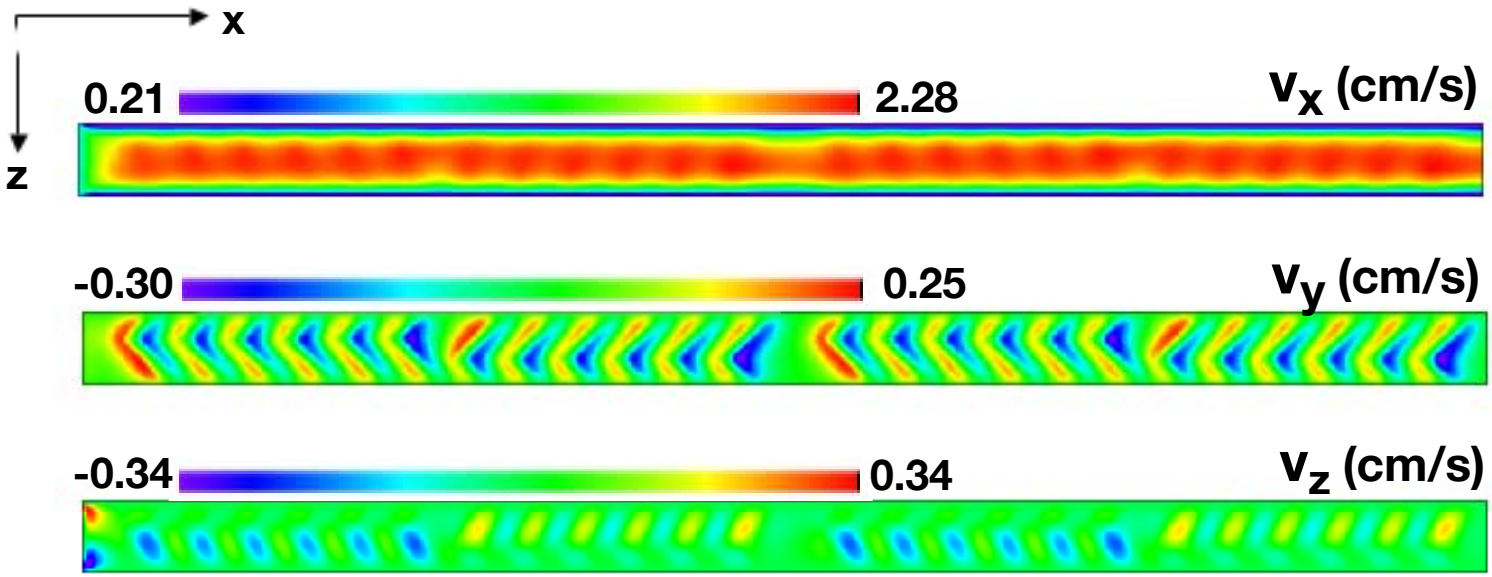

Figure 10. Velocity components at the longitudinal centerline $y = 45$ μm for the microchannel shown in Fig 1.

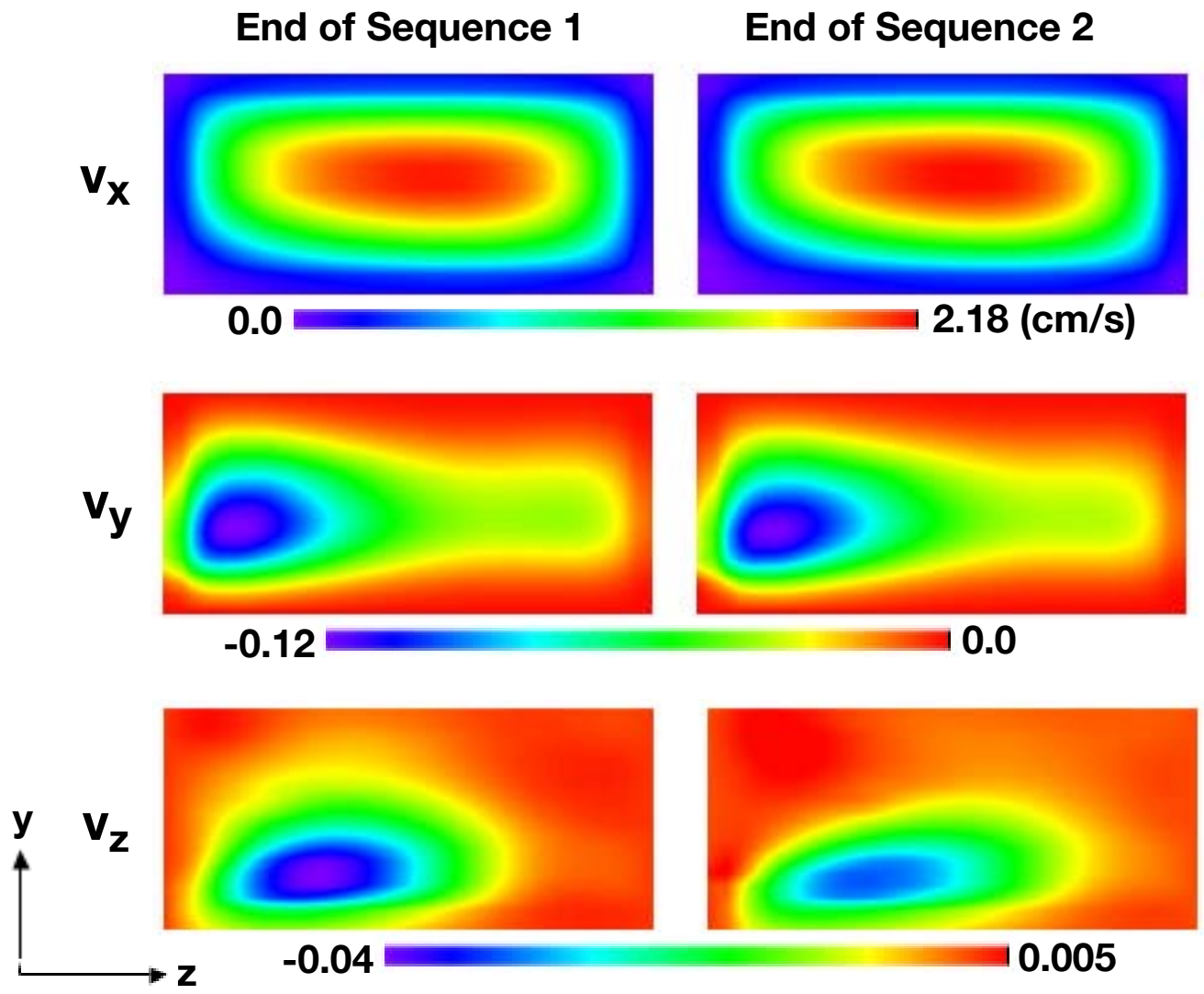

Figure 11. Velocity field at the end of sequences 1 and 2, showing that it becomes essentially periodic at the end of each sequence.

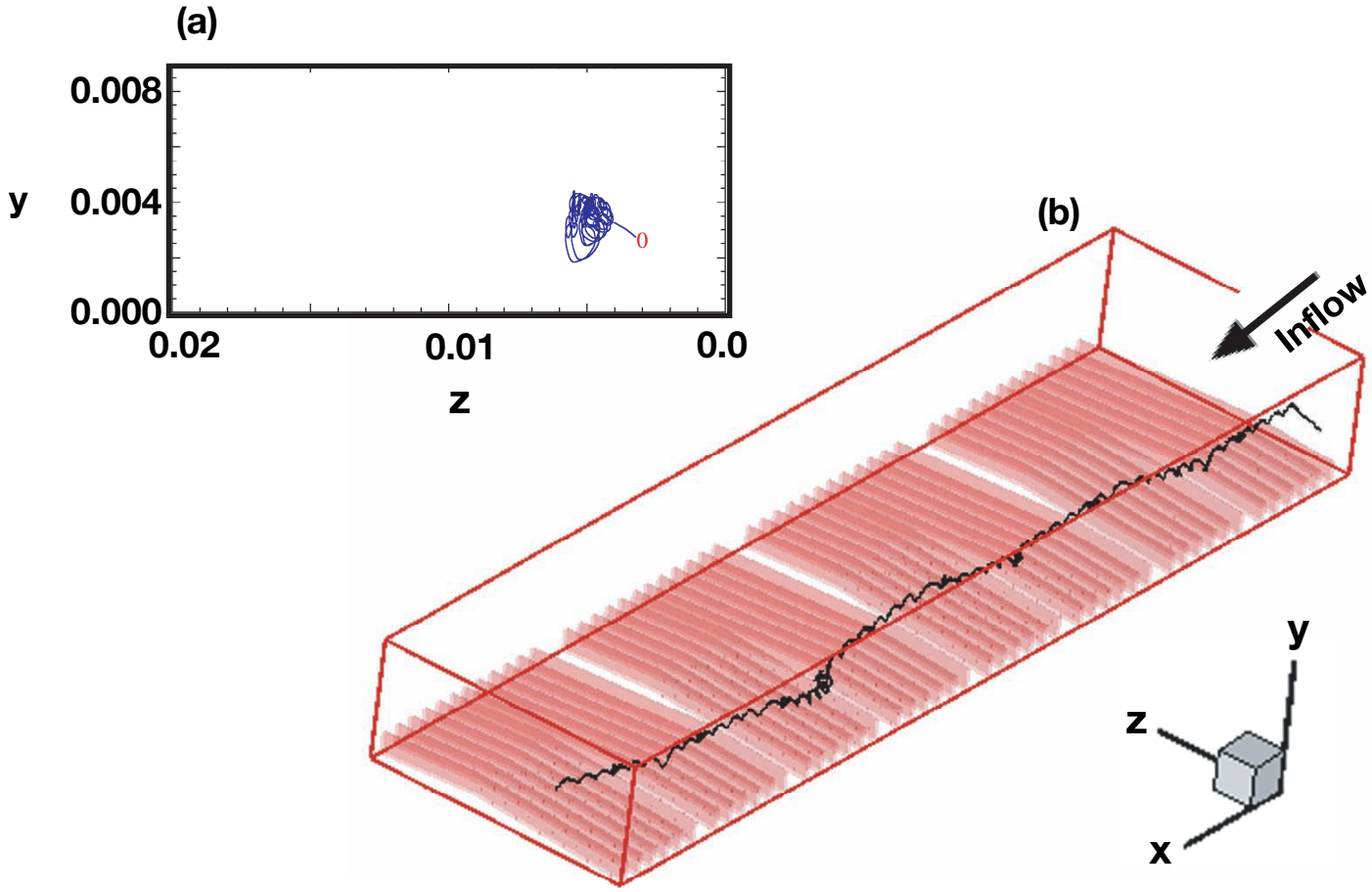

Figure 12. Track of a particle that maintains essentially the same y - z position (i.e., is essentially unaffected by the ridges) as it moves down the channel. (a) Projection on the particle path in the y - z plane. (b) Three-dimensional view of the particle motion.

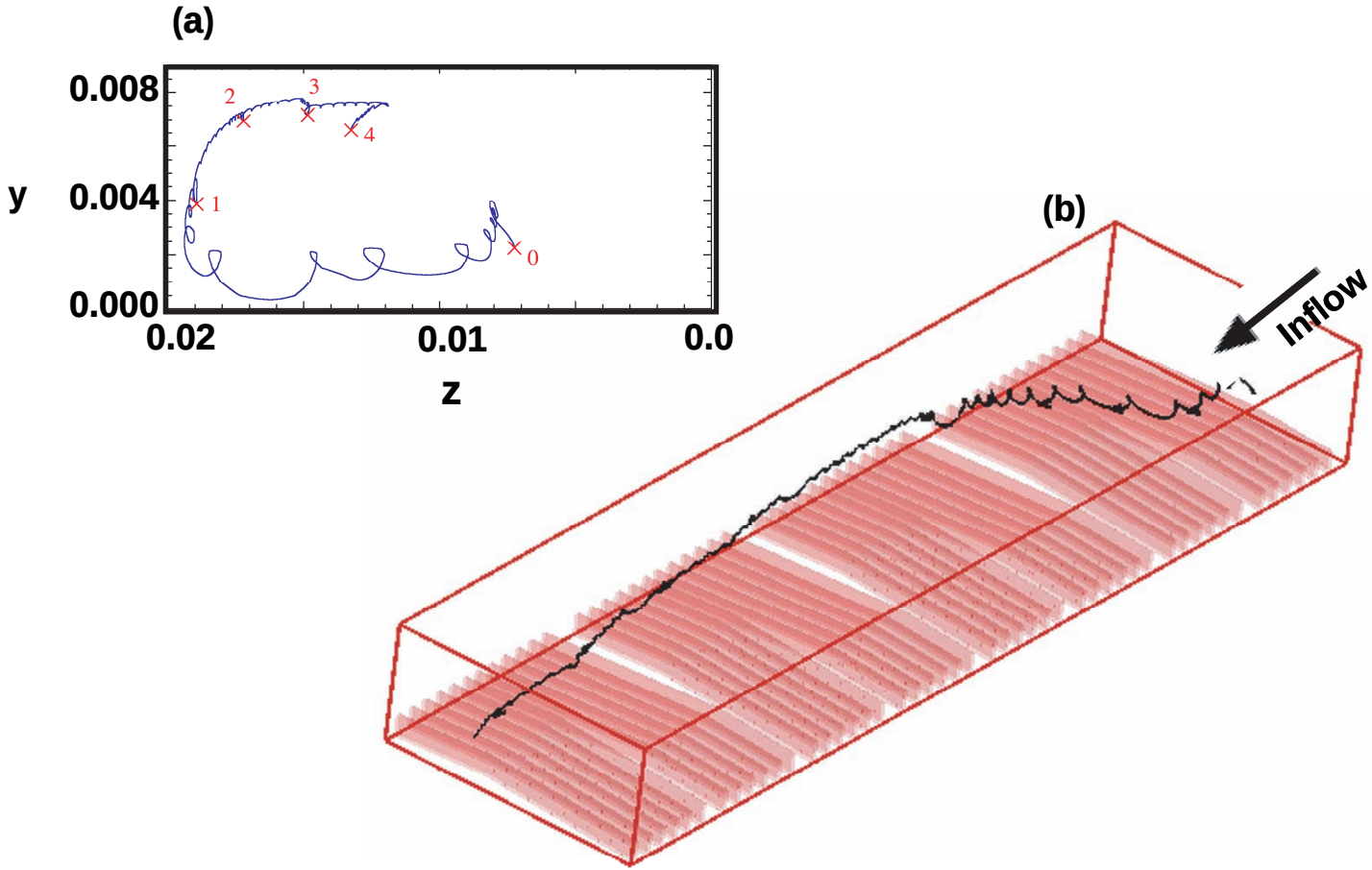

Figure 13. Track of a particle that is shifted during the first sequence to the other side as it moves down the channel. (a) Projection on the particle path in the y - z plane. The numbers in the particle projection correspond to the end of a sequence. (b) Three-dimensional view.

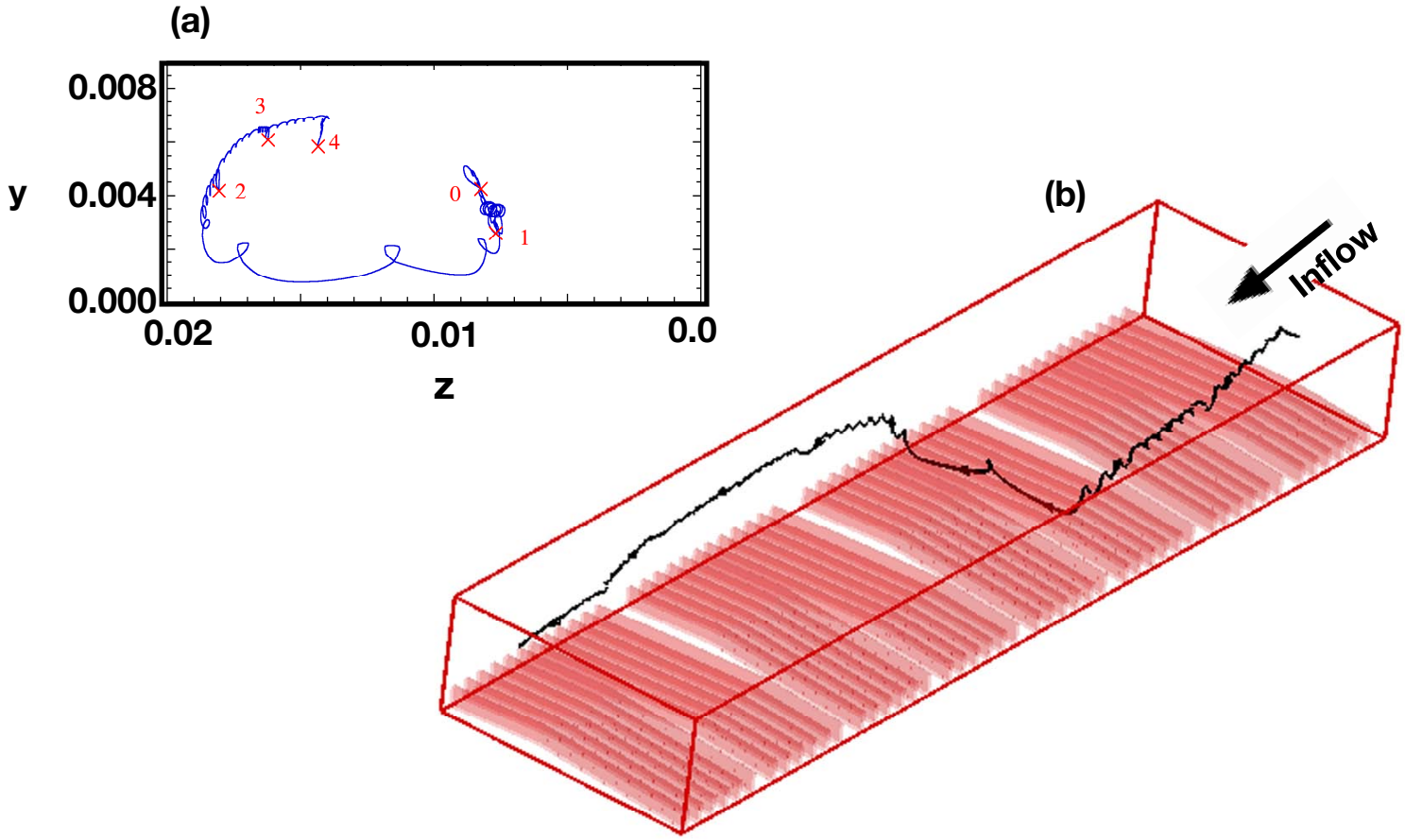

Figure 14. Track of a particle that is shifted during the second sequence to the other side as it moves down the channel. (a) Projection of the particle path in the y - z plane. (b) Three-dimensional view.

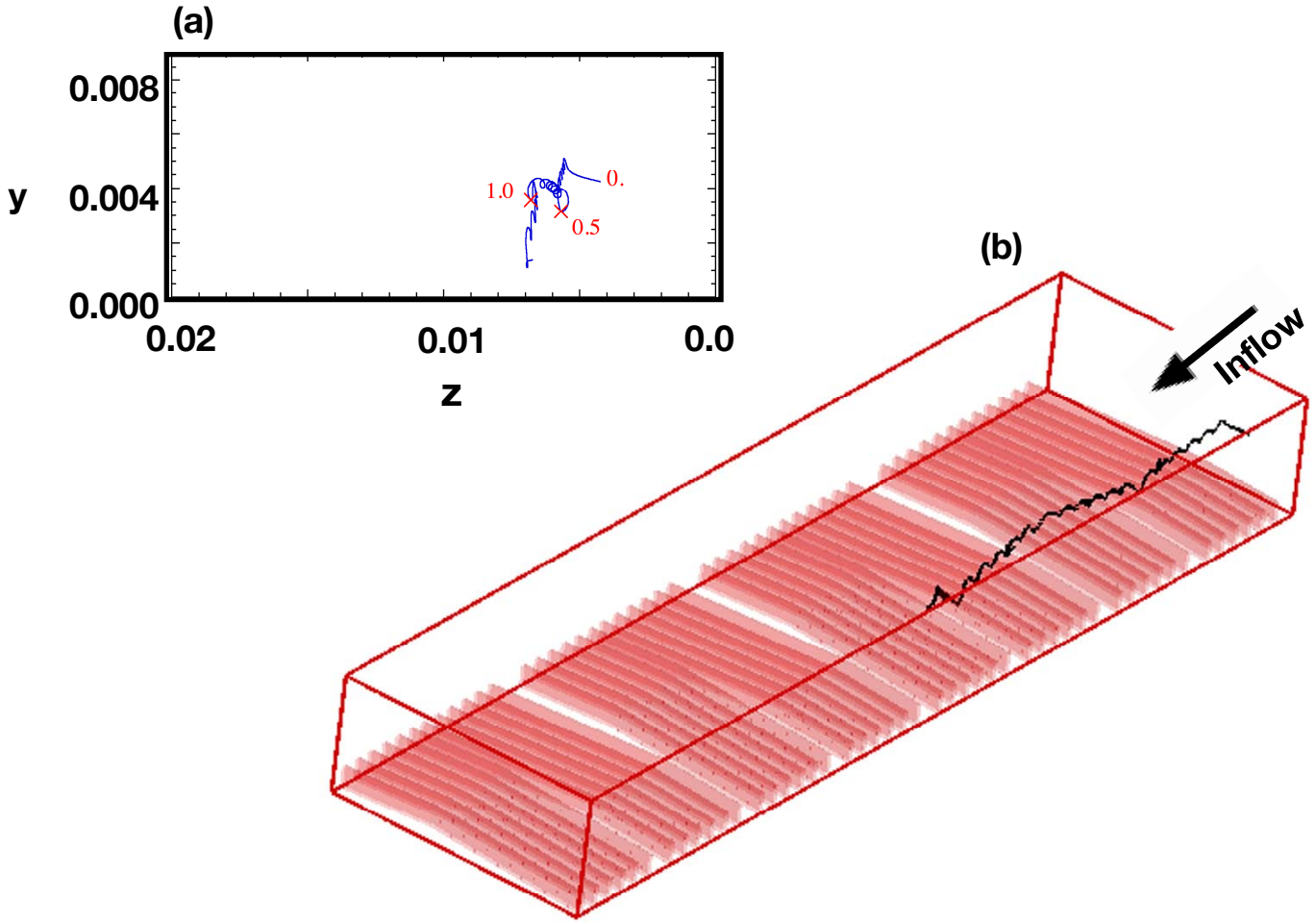

Figure 15. Track of a particle that is essentially stopped at a wall. (a) Projection on the particle path in the y - z plane. (b) Three-dimensional view.

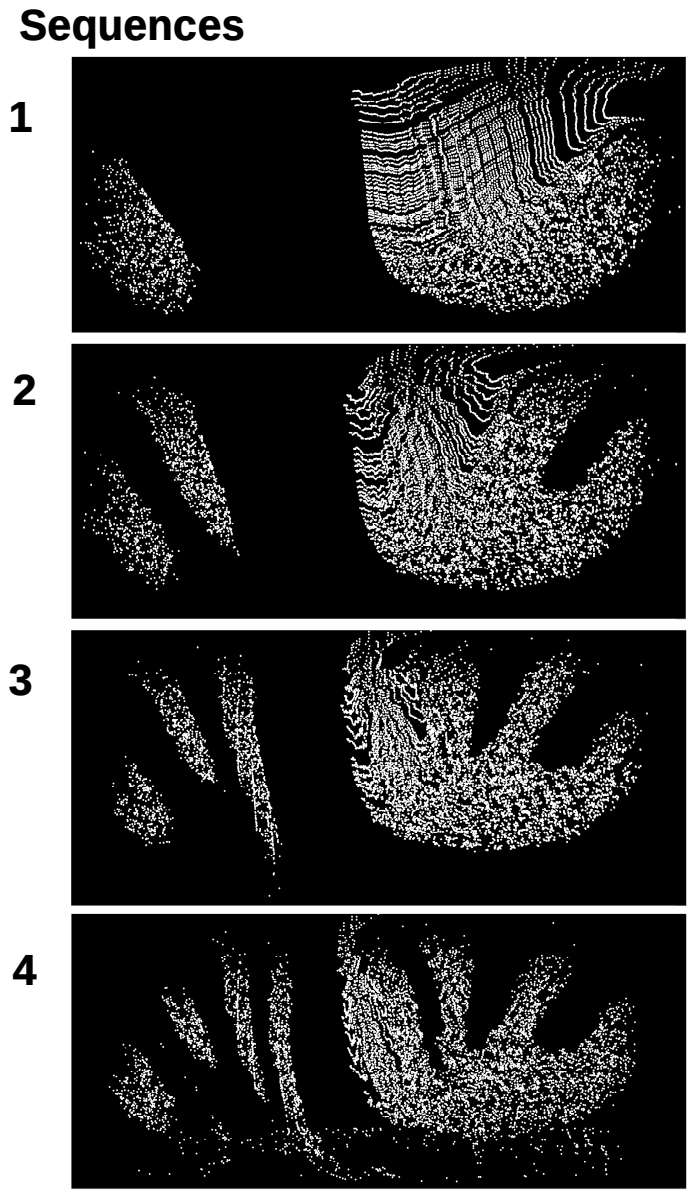

Figure 16. Poincare map showing the locations where particles B crossed the y - z plane after each sequence.

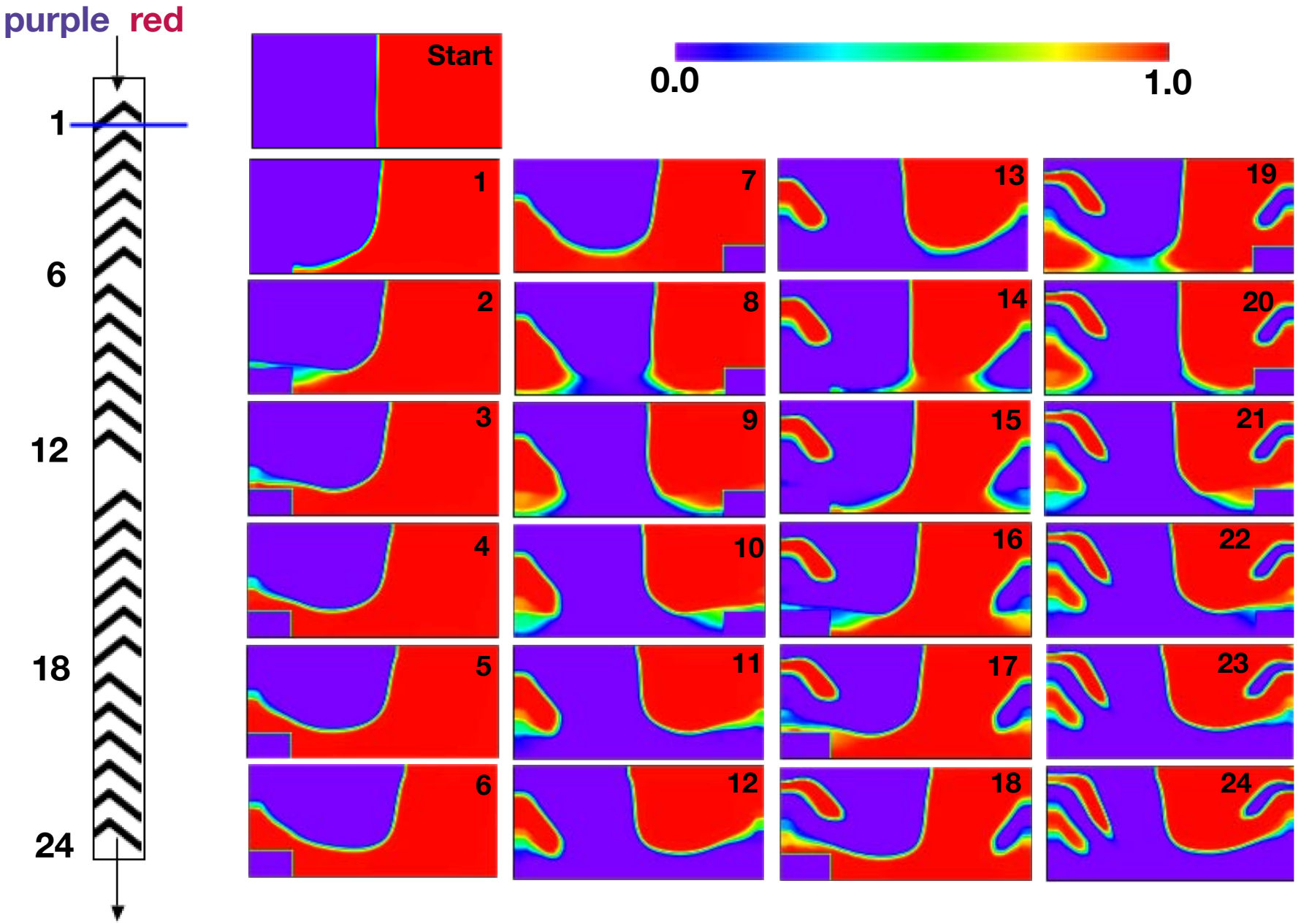

Figure 17. Concentration of passive scalars A (purple) and B (red), shown in the y - z plane, after each herringbone in the first two sequences. Computation at 1.25 μm resolution. Numbers in upper right corner of each frame (from 1 to 24) indicate locations as shown on the schematic on the left side of the figure.

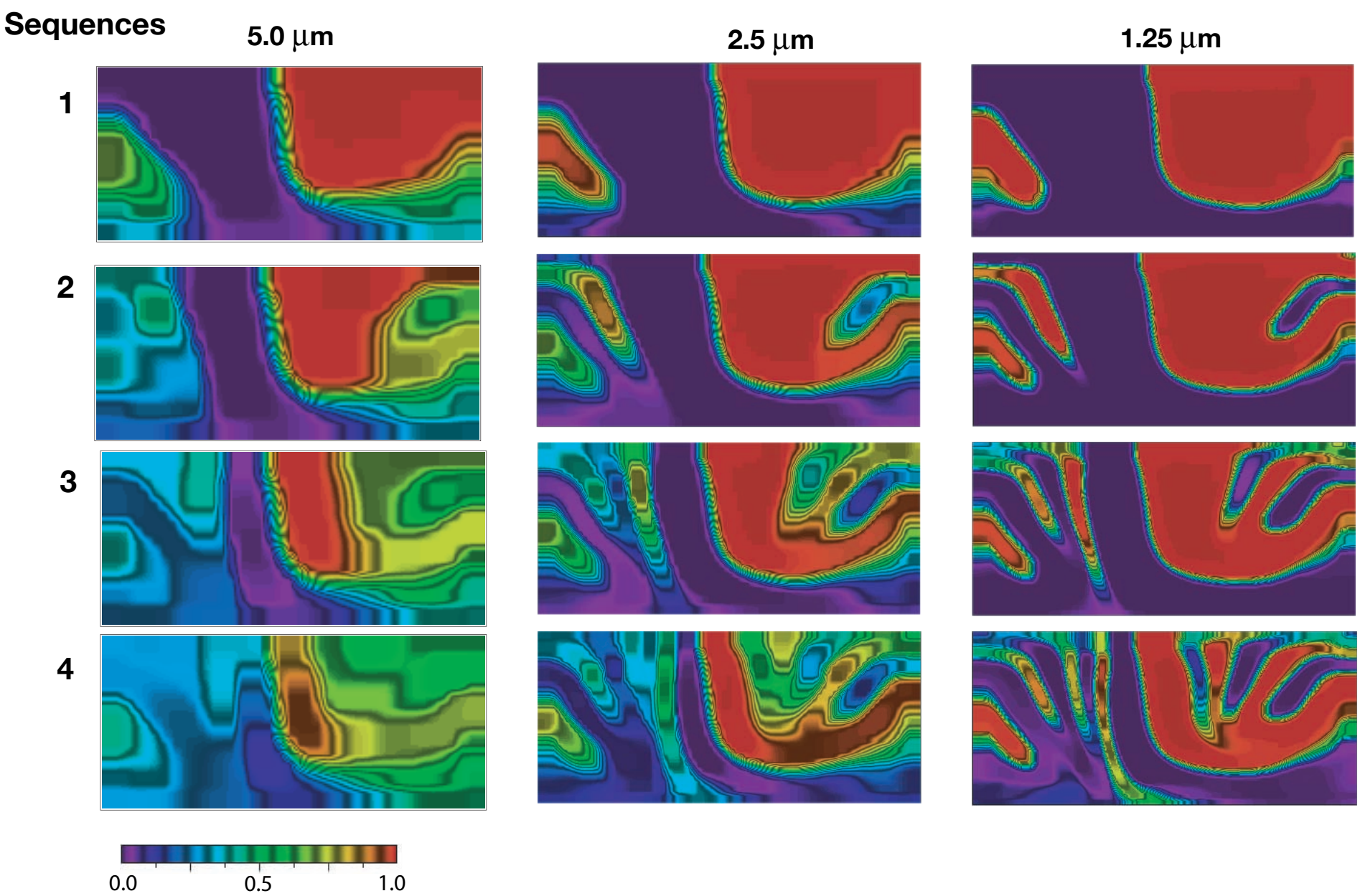

Figure 18. Concentration of passive scalars A (purple) and B (red) on the y - z plane at the end of each sequence, computed at three resolutions, using the velocity computed at 5 μm resolution.

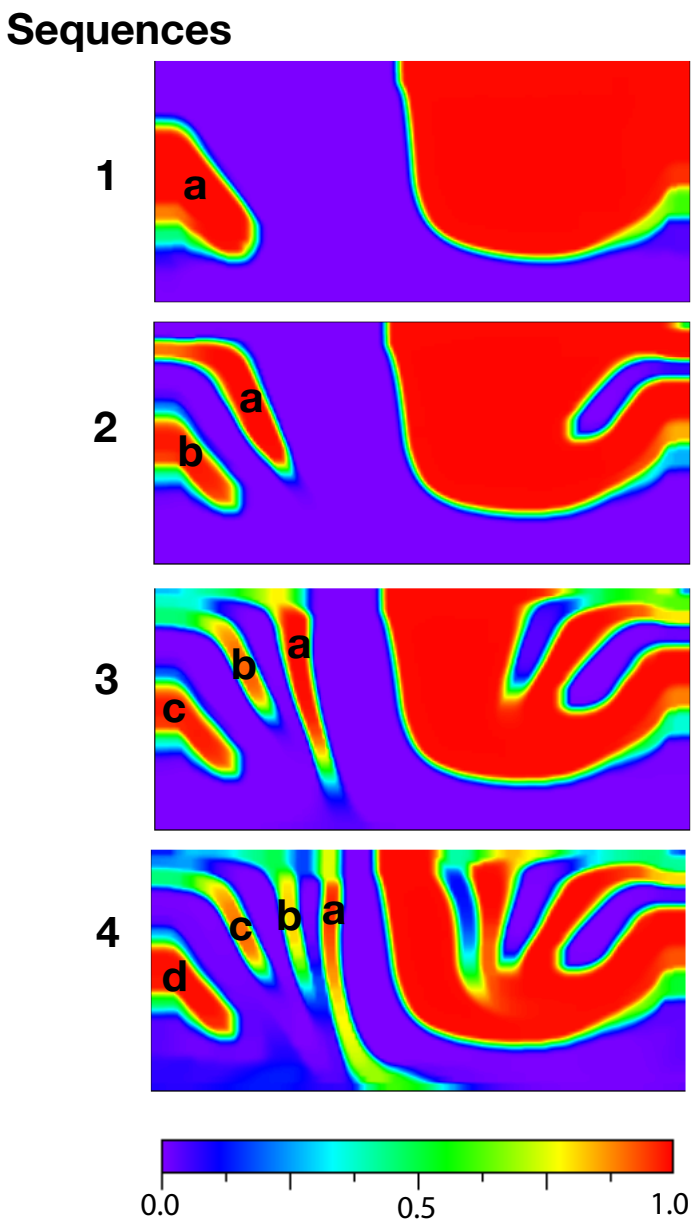

Figure 19. Concentration of passive scalars A (purple) and B (red) on the y - z plane at the end of each sequence, computed at the highest resolution (1.25 μm). Folding and stretching of fluid elements results in B being moved from the right hand side to the left hand side of the mixer. This results in the formation of island a on the left hand side at the end of first sequence. At the end of the second sequence, island b has formed on the left hand side, while island a has moved upwards and towards the center. Similar sequences of bending of folding produce islands c and d.